Developments in the Built Environment 21 (2025) 100603

Contents lists available at ScienceDirect

Developments in the Built Environment

journal homepage: www.sciencedirect.com/journal/developments-in-the-built-environment

Non-sintered artificial aggregates made of ternary alkali-activated materials with natural carbonated MSWI fly ash incorporations

Jing Gong [a], Mengmeng Wang [a], Guo Yang [b,**], Han Guo [c], Jie Yao [d], Yaxin Tao [e], Jing Zhong [c], Yubo Sun [f,*]

[a] School of Civil Engineering and Architecture, Wuhan Polytechnic University, 430023, Wuhan, China
[b] College of Civil and Transportation Engineering, Hohai University, 210098, Nanjing, China
[c] School of Civil Engineering, Harbin Institute of Technology, 150001, Harbin, China
[d] China State Construction Hailong Technology Co., Ltd., 518000, Shenzhen, China
[e] Institute for Building Materials, ETH Zurich, 8093, Zurich, Switzerland
[f] Department of Civil and Environmental Engineering, The Hong Kong Polytechnic University, 999077, China

ARTICLE INFO

Keywords:
Artificial aggregates
MSWI fly ash
Alkali-activated materials
Natural carbonation
Microstructures

ABSTRACT

This study investigates the utilization of municipal solid waste incineration (MSWI) fly ash (MFA) to produce non-sintered artificial aggregates (AAs) through alkali activation. To enhance its suitability, MFA underwent a six-month natural carbonation process to remove leachable salts and stabilize heavy metals, during which significant phase transformations were observed. The AAs were fabricated using ternary alkali-activated materials (AAMs) with varying MFA proportions through spray pelletization. Although higher MFA content reduced the strength of the AAs, this effect was counterbalanced by increasing the silicate modulus in the activators. The resulting AAs demonstrated mechanical strength comparable to or exceeding that of natural granite aggregates and recycled aggregates derived from concrete demolition waste. Furthermore, the study examined the reaction products and microstructural characteristics of the AAs. Leachate analysis confirmed compliance with environmental standards for heavy metal content, highlighting the potential of these AAs as a sustainable alternative aggregate resource for the construction industry.

1. Introduction

Natural aggregates (NAs) are one of the most significant categories among resources used in the construction sector, taking the major volume fraction to produce both Portland cement and asphalt concrete (Behera et al., 2014) (Horvath, 2004). Even though NA used to be considered an inexhaustible resource at the global scale (Ioannidou et al., 2017), the critical shortage of NA has been heeded in many regions worldwide along with the overexploitation (Habert et al., 2010) (Peduzzi, 2014), as a consequence of the rapid urbanization and booming of constructions in the past decades (Cheng et al., 2023) (Fan et al., 2020). NA is now recognized as an essential and valuable resource for worldwide social and economic development (Blengini et al., 2012). For environmental concerns, it has been reported that a few countries have restrained the extraction of NA resources (Ren et al., 2021).

To relieve the insufficient supply of NA and assure the development of construction industry, recycled concrete aggregate (RCA), produced by disassembling concrete blocks from demolition waste, has been proposed and the relevant technologies have been extensively studied over the past decades (Xiao and Xiao, 2018) (Aslam et al., 2020). However, RCA in general exhibits less-satisfactory mechanical strength, bond strength, and higher water demand over NA, and thereby limiting its broad applications (Ajdukiewicz and Kliszczewicz, 2002) (Butler et al., 2011). Meanwhile, artificial aggregate (AA) was developed as an alternative approach to producing aggregates from solid powders through pelletization or granulation (Ren et al., 2021) (Iveson et al., 2001). This is followed by hardening with calcination to enhance the bonding between fine particles while improving the mechanical properties of granules (Ramamurthy and Harikrishnan, 2006) (Wang et al., 2023), and thus could be utilized as aggregates. However, the sintering process typically adopts a temperature condition above 1000 °C from tens of minutes to a few hours, which is energy-intensive to induce extra

* Corresponding author.
** Corresponding author.
E-mail addresses: yangguoneo@hotmail.com (G. Yang), yubo.sun@polyu.edu.hk (Y. Sun).

https://doi.org/10.1016/j.dibe.2025.100603
Received 7 November 2024; Received in revised form 3 January 2025; Accepted 8 January 2025
Available online 10 January 2025

environmental impacts (Liu et al., 2023) (Gong et al., 2024). Instead, non-sintered methods (or so-called cold bonding technology) were developed to produce AA, which normally relies on cement hydration and pozzolanic reaction to achieve strength development (Gesoğlu et al., 2012), while getting rid of the high-temperature sintering process (Tang et al., 2019) (Narattha and Chaipanich, 2018). Therefore, cold bonding is considered a promising eco-friendly approach for AA production.

Another crucial issue that arises from the modern lifestyle is the vast amount of municipal solid waste (MSW) daily produced in urban communities, including household, commercial, construction, and industrial waste (Pan et al., 2015). The World Bank projects estimated that the global MSW would reach 2.2 billion tons annually in 2025 (Mian et al., 2017), resulting in great challenges in waste disposal. It has been reported that about 70% of MSW is disposed by direct landfilling in many developing countries, which leads to potential losses of resources and a great impact on underground environments (Chen et al., 2023a). With the development of waste-to-energy incineration technology, the volume of MSW has apparently declined for landfilling, whereas the heat generated could be employed for electricity generation (Kumar and Samadder, 2017) (Cheng and Hu, 2010). MSW incineration bottom ash (MBA) and fly ash (MFA) are in turn produced as major by-products to be further disposed. Previous studies have illustrated that MBA after proper treatment could be utilized as aggregates and fillers for construction materials (Stegemann et al., 1995) (Alba et al., 2001). By contrast, the application of MFA still remains problematic due to the apparently higher concentration of heavy metals and leachable salts (Yan et al., 2019) (Fan et al., 2018) and thereby categorized as a typical hazardous waste material.

In view of the environmental impact of MFA, numerous research have been carried out focusing on the solidification/stabilization (s/s) technology (Fan et al., 2024). As a common construction material, Portland cement (PC) was used as early as the 1950s to stabilize heavy metals in hazardous waste (Gesoğlu et al., 2012) (Zhang et al., 2024). With the development of alkali-activated materials (AAMs) as a green alternative to PC (Provis and Van Deventer, 2013), Jan (Deja, 2002) illustrated their superb capability of heavy metal s/s (>99.9% in Cd^{2+}, Zn^{2+}, and Pb^{2+}) due to the formation of dense gel-like reaction products, in particular while adopting sodium silicate activators. Others further reported the high efficiency in heavy metal s/s by combining various precursors and activators (Singh and Budarayavalasa, 2021) (Zhang et al., 2020). In addition, previous studies also revealed positive effects of carbonation on declining the heavy metal leaching in MFA, ascribed to the chemical bonding, physical encapsulation, as well as the variations in leaching potential (Wang et al., 2010a) (Zheng et al., 2011) (Zhang et al., 2021a). Nevertheless, MFA after s/s treatment is largely landfilled and seldom applied as an industrial raw material in practice to date (Xin et al., 2022) (Niu et al., 2022), leading to considerable losses of resources.

This study aims to investigate the potential application of MFA in producing AA. Non-sintered AAs were developed using ternary AAM mixtures containing up to 30 wt% MFA through spray pelletization. The findings indicate that heavy metal contents in AA leachate were negligible due to natural carbonation and alkali activation. The physical properties of the produced AA were thoroughly evaluated, and its compressive strength was found to be comparable to that of NA such as granite. Additionally, the reaction products and microstructural properties of AA were analyzed to elucidate the reaction mechanism. The results demonstrate that the proposed AA preparation method is an effective strategy for stabilizing heavy metals embedded in MFA while also contributing to alleviating the shortage of natural aggregate resources in the construction industry.

2. Materials and method

2.1. Materials

Commercial ground granulated blast furnace slag (BFS) and Class F coal fly ash (CFA) were utilized as the primary aluminosilicate sources for alkali activation. Additionally, municipal solid waste incineration fly ash (MFA) was introduced as a substitute precursor to partially replace CFA in the preparation of ternary alkali-activated materials (AAMs). The MFA employed in this study was sourced from a municipal solid waste incineration (MSWI) plant in Shenzhen, China, where activated carbon filtration bags were used for flue gas purification and MFA collection. The collected MFA was oven-dried at 105 °C until a constant mass was achieved for further analysis. The apparent densities of BFS, CFA, and MFA were measured to be 2800 kg/m^3, 2230 kg/m^3, and 2550 kg/m^3, respectively.

Chemical compositions of solid precursors used in this study detected with X-ray fluorescence (XRF) and loss on ignition (LOI) are presented in Table 1. Particle size distribution curves of BFS and CFA were measured with laser diffraction as shown in Fig. 1, and the results were represented as the average of three measurements. Mineralogical phase compositions of solid precursors were determined by X-ray diffraction (XRD) with the method described in section 2.5.1, as shown in Fig. 2. Mineralogical compositions of as-received MFA will be introduced in 3.1 along with the characterization after natural carbonation.

The morphology of precursors used in this study was observed with scanning electron microscopy (SEM, JOEL JSM-IT800). The SEM images were taken with the secondary electron (SE) mode with an acceleration voltage of 10 kV. For each measurement, solid grains of precursors were uniformly stuck onto a piece of conductive tape and coated with a layer of platinum to improve the conductivity before visualization. As shown in Fig. 3, angular-shaped surface morphology was observed in BFS, whereas CFA was visualized with spherical-shaped particles. By contrast, bigger particles compared to BFS and CFA were detected in as-received MFA samples, coupled with a loose matrix and suspicious organic impurities embedded in the MFA particle. Overall, characterizations on as-received MFA samples indicate that appropriate treatment is required before utilization.

Sodium hydroxide and sodium silicate were applied to prepare alkaline activators. Reagent-grade sodium hydroxide anhydrous pearls and sodium silicate solution (8% Na_2O, 27% SiO_2, and 65% water) were provided by Aladdin Co., Ltd.

2.2. Natural carbonation of MFA

Previous studies have revealed that water washing is an effective approach to remove the soluble salts in MFA (Liang et al., 2020) (Wei et al., 2022), in specific the high chloride content as illustrated in Table 1. Therefore, as-received was first washed with tap water with a liquid to solid ratio of 10:1 (L/kg) for twice to remove the soluble salts (Liang et al., 2020), and then vacuum-dried at 105 °C until constant mass. Water obtained from the washing process was collected for appropriate disposal. Dried MFA samples were then uniformly spread on a tray and kept indoors in the ambient atmosphere for six months of continuous natural carbonation. Carbonated MFA was collected after washing (WFA), as well as at the ages of two and six months (denoted as NCFA_2 and NCFA_6, respectively), and the samples were oven-dried to assess the effect of natural carbonation. Most importantly, the heavy metal leaching behaviors of as-received and carbonated MFA were evaluated according to HJ/T 300–2007 (the methods are described in detail in section 2.5). In addition, XRF and XRD analyses were conducted on carbonated MFA to check the phase evolution over time.

2.3. Mixture proportions

The mixture proportions of AAMs to prepare non-sintered AA are

Table 1
Chemical compositions of raw materials measured by XRF and LOI (by wt.%).

Precursor	CaO	SiO_2	Al_2O_3	Na_2O	MgO	SO_3	TiO_2	K_2O	Fe_2O_3	P_2O_5	Cl	Other	LOI [a]
BFS	45.97	27.62	12.91	0.42	7.92	1.65	1.79	0.44	0.43	0.03	0.06	0.76	1.27
CFA	3.41	56.53	29.18	0.40	0.76	0.63	1.60	2.31	4.39	0.21	–	0.58	0.98
MFA	50.64	1.97	0.75	5.34	0.84	4.78	0.27	5.31	1.26	1.13	26.49	1.22	3.96

[a] LOI measured by TG analysis at 950 °C.

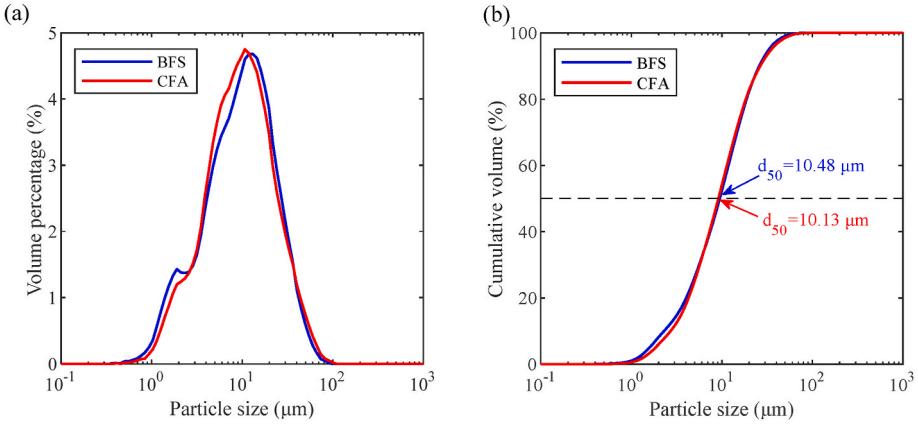

Fig. 1. Particle size distribution of solid raw materials by laser diffraction (a) Volume percentage; (b) Cumulative volume.

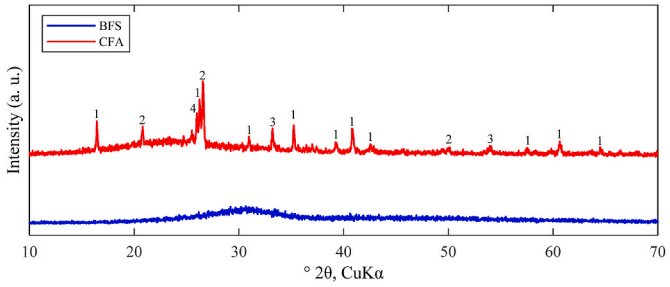

Fig. 2. Mineralogical phases of BFS and CFA by XRD analyses 1-Sillimanite ($Al_2(SiO_4)O$); 2-Quartz (SiO_2); 3-Ferric Oxide (Fe_2O_3); 4-Manganite (MnO(OH)).

presented in Table 2. These proportions were refined through a series of preliminary tests to achieve the desired consistency and mechanical properties of the AAM mixtures. A mild sodium content (3% Na_2O by mass of precursors) was applied among all AAM mixtures. M1 was designed as the reference mixture consisting of BFS and CFA precursors to assess the performance of AA with MFA incorporations. M2, M3, and M4 were prepared with an increasing MFA content (10–30% by mass of precursors) to replace CFA in AAMs. In addition, M5 and M6 were modified from M4 (30% MFA) with a varied silicate modulus (Ms) of 0 and 1 respectively, to assess the effect of activator compositions on AA properties. For all mixtures, the water to binder (w/b) ratio was kept constant at 0.22 according to preliminary tests on spray pelletization of AA with the granulator, which will be illuminated in section 2.4. It should be noted that the alkaline activators were prepared by dissolving sodium hydroxide pearls and sodium silicate solutions in tap water to reach the target compositions illustrated in Table 2. Activator solutions obtained were sealed in plastic bottles and cooled down to room temperature 24 h before mixing.

2.4. Spray pelletization

The spray pelletization method (Jiang et al., 2020) (Shi et al., 2019) was applied in this study to produce AA with ternary AAM mixtures. As shown in Fig. 4, the granulator with an inner diameter of 1000 mm and depth of 220 mm was placed with an inclination angle of 45° to the horizontal ground (Petrillo et al., 2022). AAs were prepared in batches consisting of 3000 g solid precursors and corresponding activators presented in Table 2. Solid precursors were pre-mixed with a hand-held mixer for 3 min to reach a homogeneous state before granulation. Activator solutions were loaded into a spray bottle for uniform addition into the granulator. For each mix, 2000 g blended precursors were first added into the granulator, and the rotational speed was set to 30 rpm to achieve a relatively uniform distribution of blended precursors in the granulation plate. Subsequently, approximately one-tenth of the activator solution was evenly sprinkled in 2 min to trigger the nucleation of agglomerates and bonding between precursor grains. This is followed by the gradual addition of 100 g solid precursors in the next 1 min. The 3-min sequence of activator and precursor stepwise additions was repeated in the following 30 min duration. Granular AA particles were progressively formed along with the rotation of granulation plate, due to the continuous centrifugation and gravity force. A scraper (150 × 450 mm^2, 5 mm thickness) was attached along the edge with an inclination of 60° to the granulation plate to intermix and prevent the excessive accumulation of materials. To ensure a smooth surface texture, the AA particles were further granulated at 30 rpm for 10 min after the addition of precursor and activator was completed, and the entire granulation process to produce AA takes about 40 min since the wetting of solid precursors.

AA particles obtained from the granulator were transferred into the curing device and subjected to steam curing at 80 °C for 24 h (Pan et al., 2002). Hardened AA particles were collected and sealed in plastic bags for further tests.

2.5. Testing program

2.5.1. Physical properties

The compressive strength of AA was determined by the crushing of single granular particles as proposed in previous studies (Shi et al., 2019) (Li et al., 2000). Hardened AAs with a diameter of around 10 mm were sieved out for the crushing test (Jiang et al., 2020) (Gesoğlu et al., 2007). As shown in Fig. 5, the angular AA particle was placed on the

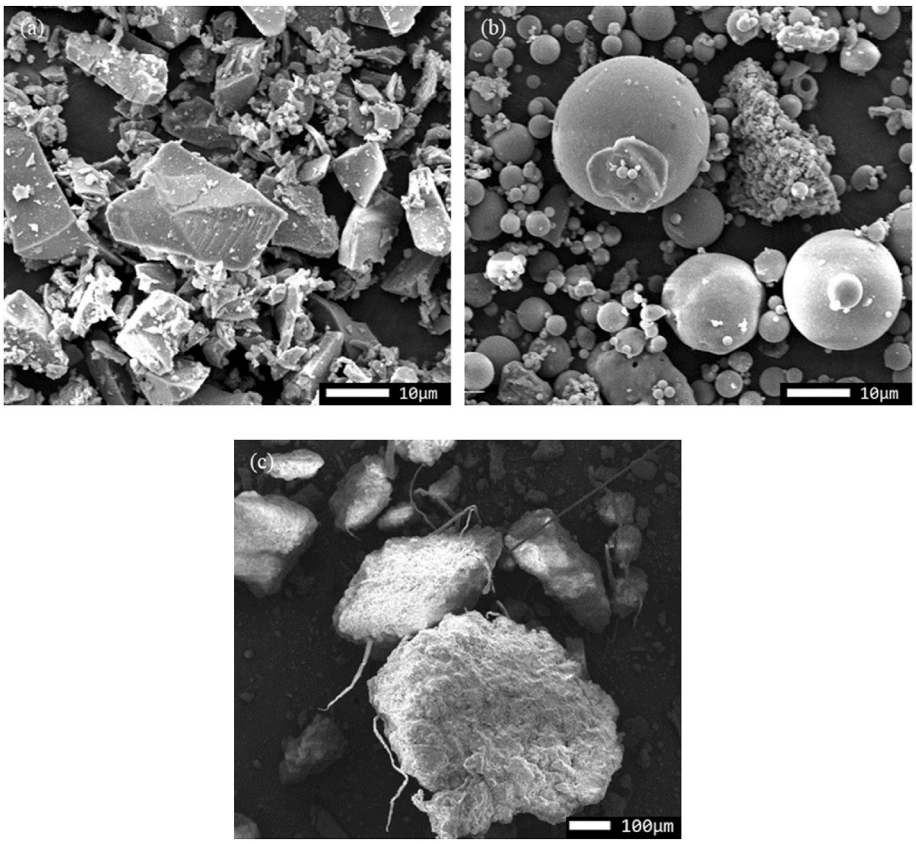

Fig. 3. Morphology of solid raw materials by SEM (a) BFS (1000 × magnification); (b) CFA (1000 × magnification); (c) as-received MFA (100 × magnification).

Table 2
Mix design of AAM mixtures used in this study (expressed as per 100 g of solid precursors).

Mix	Precursor (g)			Activator solution					w/b [c]
	BFS	CFA	MFA	Sodium hydroxide (g)	Sodium silicate solution (g)	Extra water (g)	Na_2O [a]	Ms [b]	
M1	50	50	0	3.30	5.56	19.56	3%	0.5	0.22
M2	50	40	10	3.30	5.56	19.56	3%	0.5	0.22
M3	50	30	20	3.30	5.56	19.56	3%	0.5	0.22
M4	50	20	30	3.30	5.56	19.56	3%	0.5	0.22
M5	50	20	30	3.87	0	22.87	3%	0	0.22
M6	50	20	30	2.72	11.11	16.25	3%	1.0	0.22

[a] Mass percentage by the sum of solid precursors.
[b] Molar ratio between SiO_2 and Na_2O in activators.
[c] Defined as water content in both commercial sodium silicate solution and extra water added divided by the sum of precursor and solid activators.

loading cell of a universal testing machine, and a loading rate of 1 mm/min was vertically applied until AA was crushed. The compressive strength was calculated according to Eq. (1) as proposed by Li et al. (2000), and the results were recorded as the average of 10 individual AA particles.

$$\sigma_c = \frac{2.8F_c}{\pi d^2} \tag{1}$$

where σ_c is the compressive strength of AA (MPa); F_c is the loading applied at failure (N); and d is the average diameter of AA obtained from three axial measurements (mm).

Other physical properties of AA produced in terms of bulk density and water absorption were determined with the methods described below. Results presented were taken as the average of three measurements. The bulk density of AA samples was measured with a balance and measuring cylinder. The mass of AA was first measured at room temperature and recorded as m. A certain amount of water was then added into the measuring cylinder, and recorded as V_1. Followed by submerging the AA sample in the measuring cylinder, and the volume of water after AA addition was recorded as V_2. The bulk density of AA was determined with Eq. (2).

$$\rho = \frac{m}{V_2 - V_1} \tag{2}$$

where m is the mass of the AA sample (g); V_1 is the volume before submerging (mL); V_2 is the volume after AA submerging (mL).

Apart from that, the water absorption of AA was also determined in parallel. AA samples were oven-dried at 105 °C until constant mass and recorded as m_1. Subsequently, AA particles were immersed in water at room temperature for 24 h. Testing samples were then collected from the water and wiped with a clean absorbent cloth until no visible water film on the surface. The mass of saturated surface-dry AA samples was recorded as m_2. Eventually, the water absorption of AA can be calculated with Eq. (3).

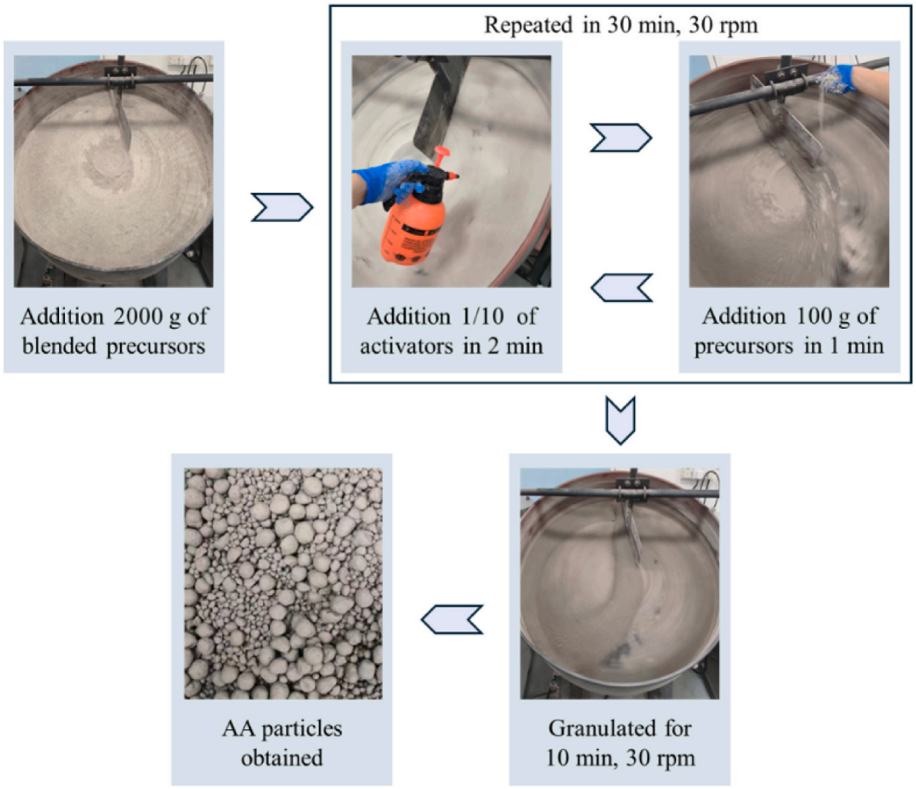

Fig. 4. Preparation of AAs through spray pelletization.

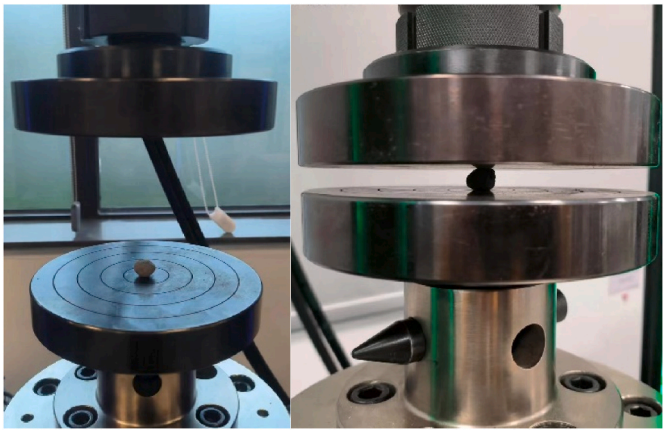

Fig. 5. Crushing test on the compressive strength of AA particles with the universal testing machine.

$$W = \frac{m_2 - m_1}{m_1} \times 100\% \quad (3)$$

where m_1 is the mass of oven-dried AA samples (g); m_2 is the mass of saturated surface-dried AA samples (g).

2.5.2. Heavy metal leaching behaviors

The leaching of heavy metals in AA was determined in line with HJ/T 300–2007 to assess the efficiency of s/s by adopting AAMs. The extractant was prepared by diluting 17.25 mL of glacial acetic acid with de-ionized water to 1 L (pH = 2.65). AA particles collected from the crushing test (<3 mm) were oven dried at 60 °C for 24 h, and loaded into a plastic bottle filled with the extractant with a liquid to solid ratio of 20:1(L/kg) (Shao et al., 2021). The bottle was then sealed and placed on a roller and vibrated at 30 rpm for 18 h. The supernatant obtained was extracted with a syringe to pass through a 0.75 μm fiberglass membrane filter. The hazardous content in leachate was then analyzed with an inductively coupled plasma optical emission spectrometry (ICP-OES, Thermo Fisher Scientific iCAP RQ) to determine the concentration of Cu, Zn, Cd, Cr, Pb, and Ni heavy metals (C. Ag- and B. C. 127-15 Statements et al.).

2.5.3. Reaction products

Reaction products were characterized on hardened AA samples after steam curing. In specific, AA particles obtained were split into smaller pieces and submerged in isopropanol to arrest the alkali activation reaction (Palacios et al., 2021) (Sun et al., 2023). Solid samples were collected by vacuum filtration, and further ground with an agate mortar to pass through the 63 μm sieve. The fine powder obtained was transferred into a desiccator under vacuum until constant mass. Samples were sealed in plastic bags and placed in a vacuum chamber for subsequent characterizations with XRD and thermogravimetric (TG) analyses.

XRD analyses were first conducted to detect the mineralogical composition of reaction products in AAMs, using a Bruker D8 Advance diffractometer with Cu-Kα radiation (λ = 1.54 Å). XRD patterns were detected between 10° and 70° with a step size of 0.02°. In parallel, TG analyses (TGA) were performed with a Netzsch TG209F3 instrument to provide quantitative characterizations on the reaction products formed in AAMs. For each sample, approximately 50 mg of the solid powder was loaded into an Al_2O_3 crucible, and then incinerated in an argon atmosphere from 30 to 1000 °C with a heating rate of 10 °C/min. The mass loss was recorded along with the increase in temperature for analysis. XRD and TGA tests in this study were conducted twice to check the repeatability.

2.5.4. Microstructural properties

SEM tests were performed on fracture and polished surfaces of hardened AA samples to investigate the microstructural properties. Crushed AA particles were treated with isopropanol to terminate the

activation reaction, as indicated in the previous section. Followed by vacuum filtration and drying until constant mass. AA particles after drying were subjected to surface treatment for visualization with SEM. AA samples for the polished surface were first vacuum impregnated with a low-viscosity epoxy. The block particles were then ground and polished using abrasive papers and diamond lapping paste embedded in polishing clothes to reach a smooth surface up to 0.25 μm surface fineness (Wong and Buenfeld, 2006) (Sun et al., 2024a).

For samples of both fracture and polished surfaces, a thin layer of platinum was coated onto the sample to improve the conductivity for visualization. Microstructural visualization was carried out using a JOEL JSM-IT800 SEM in low vacuum conditions. Energy dispersive X-ray spectroscopy (EDX) analyses were performed on SEM images to assess the elemental composition in microstructures, which were taken with the backscattered electron (BSE) mode with an accelerating voltage of 10 kV.

3. Results and discussion

3.1. Natural carbonated MFA

Chemical compositions of MFA samples were characterized by XRF analysis, as listed in Table 3. Results show that the chloride content declined by 74.3% after washing with water, coupled with significant reductions in sodium and potassium content. In the meantime, the concentration of other elements slightly improved. It can be inferred that the leachable chloride salts were effectively removed by water. Moreover, no apparent variations in the chemical compositions were detected along with the natural carbonation process. Mineralogical phases developed in carbonated MFA samples are presented in Fig. 6. Numerous chloride binding phases (e.g. sylvite, halite, calcium chloride hydroxide, etc.) were detected in the as-received MFA, referring to the high chloride content shown in Table 3. However, the relevant phases nearly vanished after water washing and carbonation, accompanied by the reduction in portlandite phases (Wang et al., 2010b). In turn, the characteristic phases of calcite located at around 29.5° (other minor peaks along the XRD patterns as well) progressively intensified along the natural carbonation, indicating the CO_2 uptake attributed to the portlandite phases originated from MFA (Gao et al., 2024) (Ren et al., 2024).

The heavy metal leaching behaviors of MFA samples are shown in Table 4. It was found that Zn, Cd, Pb, and Ni in as-received MFA have almost reached or exceeded the upper limits indicated in GB standards. Results above have illustrated that the heavy metal leaching from MFA was gradually mitigated after treatment through washing and natural carbonation, among which the s/s effect became more pronounced with increases in the natural carbonation duration, through which a dense layer of calcium carbonate is formed on MFA surfaces to achieve physical encapsulation (Fig. 7 (b)) (Chen et al., 2023b). Moreover, leachates of heavy metal oxides were precipitated due to the declined alkalinity along with the carbonation process, improving the leaching behavior of carbonated MFA (Chen et al., 2022). Therefore, it was decided to produce AAs with ternary AAM mixtures using MFA-6 samples (denoted as MFA in this work hereafter), and for further s/s of the heavy metal content.

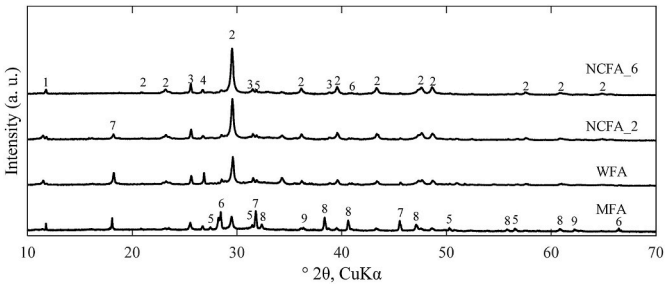

Fig. 6. Mineralogical phases in as-received and natural carbonated MFA samples by XRD analyses (1-Gypsum ($Ca(SO_4)(H_2O)_2$)); 2-Calcite ($CaCO_3$); 3-Anhydrite ($CaSO_4$); 4-Quartz (SiO_2); 5-Halite (NaCl); 6-Sylvite (KCl); 7-Portlandite ($Ca(OH)_2$); 8-Calcium chloride hydroxide (CaClOH)); 9-Magnetite (Fe_3O_4).

Table 4
Heavy metal leaching of MFA samples with respect to the upper limit in GB Standards (mg/L).

	Cu	Zn	Cd	Cr	Pb	Ni
MFA	6.271 ±0.040	127.797 ±0.814	3.869 ±0.427	0.513 ±0.004	2.313 ±0.095	2.030 ±0.102
WFA	6.009 ±0.138	120.386 ±2.134	3.617 ±0.558	0.496 ±0.012	2.117 ±0.063	1.886 ±0.132
NCFA_2	4.721 ±0.081	99.708 ±1.012	2.915 ±0.041	0.339 ±0.004	1.327 ±0.084	1.795 ±0.086
NCFA_6	3.330 ±0.034	88.101 ±0.696	2.655 ±0.019	0.273 ±0.007	0.841 ±0.010	1.176 ±0.205
Standard [a]	120	120	0.6	15	1.2	2
Standard [b]	100	100	1	15	5	5
Standard [c]	40	100	0.15	4.5	0.25	0.5

[a] GB 18598-2019: Standard for pollution control on the hazardous waste landfill.
[b] GB 5085.3-2007: Identification standard for hazardous waste - Identification for leaching toxicity.
[c] GB 16889-2008: Standard for pollution control on the landfill site of municipal solid waste.

As shown in Fig. 7 (a), carbonated MFA was ground with a high-speed grinding machine to reach a similar particle size distribution as BFS and CFA (Fig. 1). MFA was detected with an angular surface morphology similar to that of BFS (Fig. 3), while smaller powders were attached to the surface of larger grains (Fig. 7 (b)), which aligns with the finer particle size distribution of MFA compared to BFS as indicated by the laser diffraction analysis (Fig. 7 (a)).

3.2. Physical properties

The results of crushing tests are shown in Fig. 8. In addition, NA (granite) and RCA available in the local market were tested in parallel for comparison. The compressive strength of granite NA and RCA was measured at 5.47 MPa and 2.48 MPa, respectively, aligning with values commonly reported in the literature (Park et al., 2018) (Song et al.,

Table 3
Chemical compositions of as-received and natural carbonated MFA by XRF and LOI (by wt.%).

	CaO	SiO_2	Al_2O_3	Na_2O	MgO	SO_3	TiO_2	K_2O	Fe_2O_3	ZnO	P_2O_5	Cl	Others
MFA	50.64	1.97	0.75	5.34	0.84	4.78	0.27	5.31	1.26	1.13	0.21	26.49	1.01
WFA	70.37	3.86	1.45	0.25	1.82	6.60	0.60	1.21	2.70	2.30	0.42	6.81	1.63
NCFA_2	70.43	3.96	1.44	0.24	1.88	6.65	0.58	1.18	2.78	2.35	0.42	6.44	1.64
NCFA_6	71.92	3.84	1.45	0.18	1.79	6.61	0.63	1.06	2.76	2.37	0.43	5.35	1.62

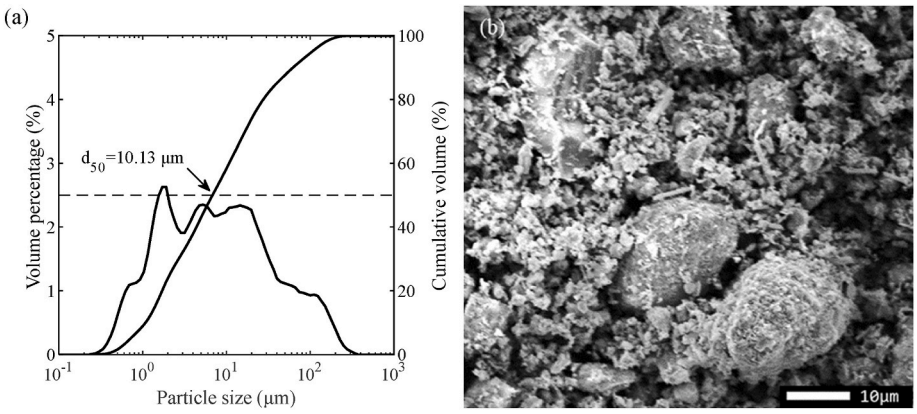

Fig. 7. Physical properties of MFA (a) Particle size distribution; (b) Morphology by SEM (1000 × magnification).

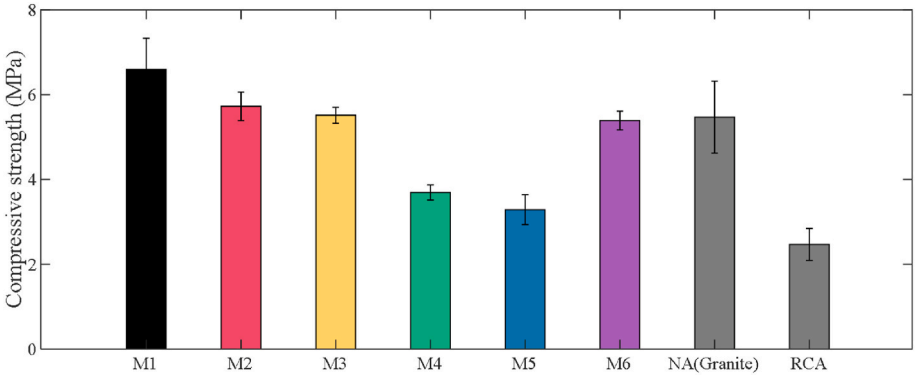

Fig. 8. Compressive strength of AAs, NA (Granite), and RCA from concrete demolition waste.

2023) (Ren et al., 2021). However, it is important to acknowledge that the properties of NA and RCA might vary depending on their sources and testing conditions. AAs in general exhibit satisfying mechanical performance with a higher or similar compressive strength compared to natural granite aggregates. The highest strength of 6.6 MPa was detected in M1 among all mixtures. Moreover, the compressive strength of AA declined by 13.2% in M2 with 10 wt% MFA inclusion, and further reduced with higher MFA replacement levels. It was found that the M5 with the highest MFA content of 30 wt% and activated with sodium hydroxide activators exhibited the worst mechanical property, which was still 33% higher than that of RCAs. By contrast, the compressive strength of AAs progressively improved with the increase of Ms in activators. This is attributed to the nucleation effect of silicate species (Duxson et al., 2005) (Gebregziabiher et al., 2015), leading to the formation of a denser AAM matrix (Sun et al., 2022).

Apart from that, physical properties in terms of apparent density and water absorption of AAs are summarized in Table 5. Results follow the same trend as the strength of AA particles. The apparent density of AA particles gradually declined with an increased MFA dosage in mix design, accompanied by a higher rate of water absorption rate. On the other hand, the AA particles became denser accompanied by a reduced water absorption rate along with the increase in Ms of activators.

3.3. Leaching behaviors

The heavy metal leaching behaviors were investigated on crushed pieces of AA particles, as presented in Table 6, to ensure environmental safety. It was found that the Cu, Zn, Cr, and Ni content detected in the leachate significantly declined compared to naturally carbonated MFA (Table 6). In addition, Cd and Pb were hardly found in a few mixtures. AA produced with ternary AAM mixtures containing carbonated MFA exhibited promising s/s efficiency, and various heavy metal contents were far below the limitations indicated in GB standards. The s/s efficiency of AAs was further evaluated with respect to the leached metals from as-received and carbonated MFA samples (Fan et al., 2021), as presented in Fig. 9. Results further illustrated that the natural carbonation and alkali activation approach employed showed satisfying s/s performance in Cu, Zn, Cd, and Pb heavy metals, with the s/s efficiency exceeding 99% among all mixtures. By contrast, Cr and Ni were less stabilized with the method proposed, in particular in M4 and M5 with a higher MFA content and low MS in activators. A limited capability of Cr s/s was observed compared to other heavy metals by adopting alkali activation, which is in agreement with previous research (Liu et al., 2021). The reaction products and microstructural properties of AAs were further investigated to investigate the interactions between the AAM binder and heavy metals in the following sections.

Table 5
Apparent density and water absorption of AAs.

	M1	M2	M3	M4	M5	M6
Apparent density (kg/m^3)	1788.38±2.67	1767.31±2.60	1719.21±4.93	1671.32±4.66	1621.70±7.41	1769.93±5.22
Water absorption (%)	8.70±0.10	8.98±0.20	9.23±0.02	10.97±0.11	11.30±0.03	9.09±0.14

Table 6
Heavy metal leaching of AA particles with respect to the upper limit in GB Standards (mg/L).

Mix	Cu	Zn	Cd	Cr	Pb	Ni
M2	0.0020±0.0004	0.0563±0.0032	–	0.0860±0.0051	–	0.0615±0.0085
M3	0.0030±0.0009	0.1429±0.0445	–	0.1212±0.0087	–	0.1117±0.0200
M4	0.0040±0.0005	0.3647±0.0326	0.0023±0.0008	0.1441±0.0080	–	0.1615±0.0120
M5	0.0196±0.0135	0.4823±0.0309	0.0030±0.0008	0.1414±0.0046	0.0048±0.0044	0.2609±0.0034
M6	0.0066±0.0012	0.3629±0.0345	–	0.1176±0.0068	0.0015±0.0003	0.1291±0.0047
Standard [a]	120	120	0.6	15	1.2	2
Standard [b]	100	100	1	15	5	5
Standard [c]	40	100	0.15	4.5	0.25	0.5

'-' denotes not detected.
[a] GB 18598-2019: Standard for pollution control on the hazardous waste landfill.
[b] GB 5085.3-2007: Identification standard for hazardous waste - Identification for leaching toxicity.
[c] GB 16889-2008: Standard for pollution control on the landfill site of municipal solid waste.

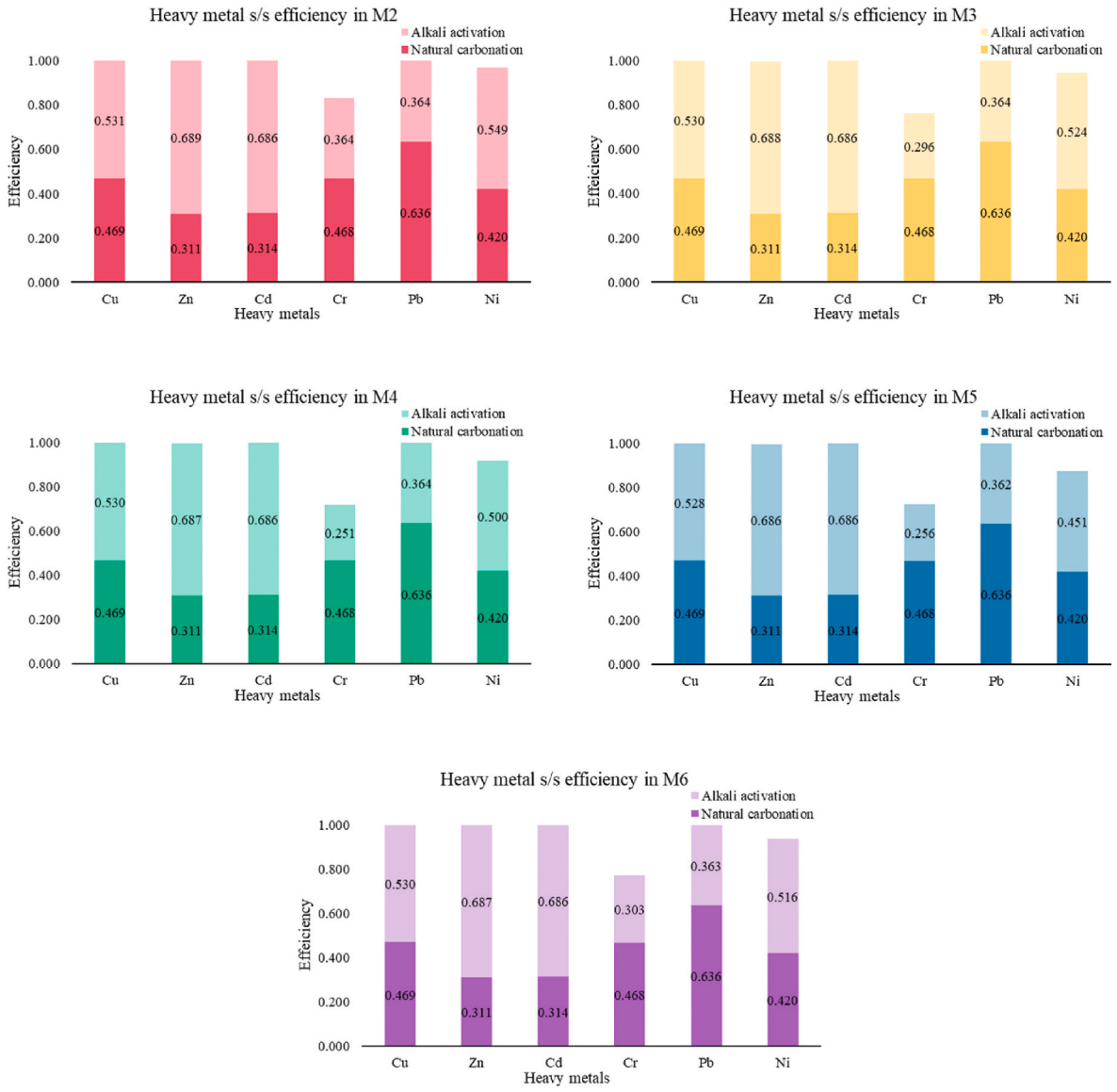

Fig. 9. Heavy metal s/s efficiency in AAs by adopting natural carbonation and alkali activation.

3.4. Reaction products

XRD patterns of AA samples are plotted in Fig. 10 to reveal the mineralogical phases developed after steam curing of AAMs. The diffuse humps distributed between 29° and 33° 2θ confirmed the formation of amorphous C-(N-)A-S-H reaction products during activation reactions (Ben Haha et al., 2011a) (Kulasuriya et al., 2014). Results further revealed that the sharp characteristic peak of calcite located at around 29.5°, as well as other calcite peaks distributed along the testing region apparently intensified with the increase in MFA replacement ratio, and

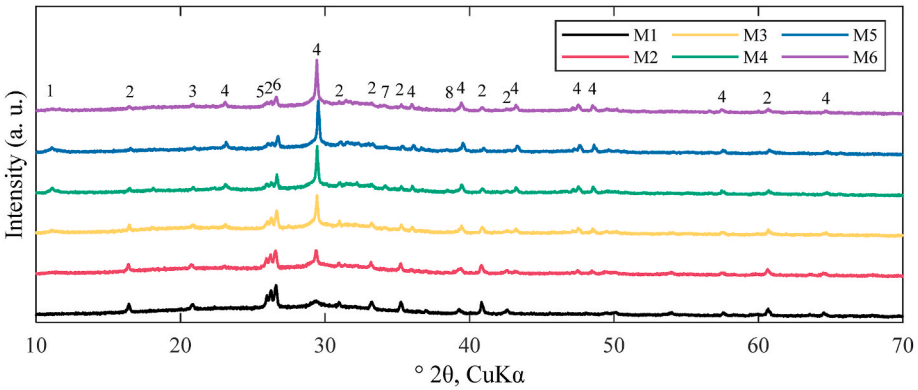

Fig. 10. Mineralogical phases in AAs by XRD analyses (1-Hydrotalcite ($Mg_6Al_2CO_3(OH)_{16}{\cdot}4H_2O$)); 2-Sillimanite ($Al_2(SiO_4)O$); 3- Åkermanite ($Ca_2MgSi_2O_7$); 4-Calcite ($CaCO_3$); 5-Manganite ($MnO(OH)$); 6-Quartz ($SiO_2$); 7-Portlandite ($Ca(OH)_2$); 8-Anhydrite ($CaSO_4$)).

became predominant in M4, M5, and M6. This is accompanied by the increase in other characteristic phases from MFA, as shown in Fig. 10. On the other hand, mineral phases originated from CFA (e.g. sillimanite, quartz, orthoclase, and manganite) turned less significant with the gradual substitution with MFA. It should be noted that other minor phases featured in Fig. 6 with trace content were less evident due to the predominance of calcite, and thus not discussed in this paragraph.

TG analyses were carried out to evaluate the reaction products formed in AA samples. The mass evolution and differential thermogravimetry (DTG) profiles as a function of temperature are displayed in Fig. 11. The major mass losses in AA samples can be categorized into the following three stages: (1) decompositions of C-(N-)A-S-H phases below 200 °C (Garcia-Lodeiro et al., 2011) (Kapeluszna et al., 2017); (2) dehydrations of hydrotalcite phases from 200 to 400 °C (Ben Haha et al., 2011a) (Ismail et al., 2014); and (3) decomposition of carbonated phases between 500 and 800 °C (Sun et al., 2024b). In addition, some minor peaks observed above 800 °C could be attributed to the formation of minor crystalline phases (e.g. Åkermanite) (Rovnaník et al., 2013) (Zhang et al., 2021b).

As illustrated in Fig. 11 (a), the primary peak in DTG profiles corresponding to C-(N-)A-S-H gels apparently declined with a higher MFA content, revealing the adverse effect of MFA on the alkali activation reactions. Instead, the peak referring to carbonated phases located at around 700 °C progressively intensified as more MFA was incorporated, which was associated with the extensive calcite phases distributed in MFA after natural carbonation. In the meantime, results also suggest that more hydrotalcite phases were formed along with the increase in MFA content, in line with the corresponding XRD peaks presented in Fig. 10. It can be seen that the magnesium content in MFA was apparently higher than that of CFA, which promoted the incorporations of Mg elements into reaction products (Le Saoût et al., 2011) (Ben Haha et al., 2011b). In addition, results of mixtures with various Ms in activators are shown in Fig. 11 (b). It was found that the silicate species have facilitated the formation of the primary reaction product, resulting in a more intensive peak corresponding to C-(N-)A-S-H gels in M6 compared to M4. M6 with a denser matrix in turn exhibited a more pronounced effect on the encapsulation of heavy metals over other mixtures. By contrast, C-(N-)A-S-H gels were less detected in M5 with the absence of silicate species in activators. Besides, the minor peaks located at about 400 °C slightly declined with a higher Ms, in line with previous studies that hydrotalcite phases were less accumulated in AAMs with a higher silicate dosage in activators (Ben Haha et al., 2011c) (Sun et al., 2023). Moreover, the relevant carbonated phases maintained a similar level in M4, M5, and M6, due to the identical MFA content in these mixtures.

3.5. Microstructural properties

SEM images (Figs. 12 and 13) were taken to investigate the microstructural properties. AA particles exhibit distinct morphologies on fracture surfaces by using different mixture proportions. As shown in Fig. 12 (a), angular BFS and spherical CFA grains could be clearly identified in the reference mix M1, embedded under a layer of uniform fluffy gel structures. This can be ascribed to the amorphous C-(N)-A-S-H gels formed in AAs (Kim, 2019) (Cao et al., 2020), which are recognized as the primary reaction products in alkali-activated BFS and CFA mixtures (Provis and Bernal, 2014). Further, solid grains with finer particle sizes were observed with the addition of MFA, and these particles were less covered with the amorphous reaction products, indicating a less reactive nature compared to other precursor grains. Calcite crystals were observed with the gradual addition of MFA, as represented in Fig. 12 (e),

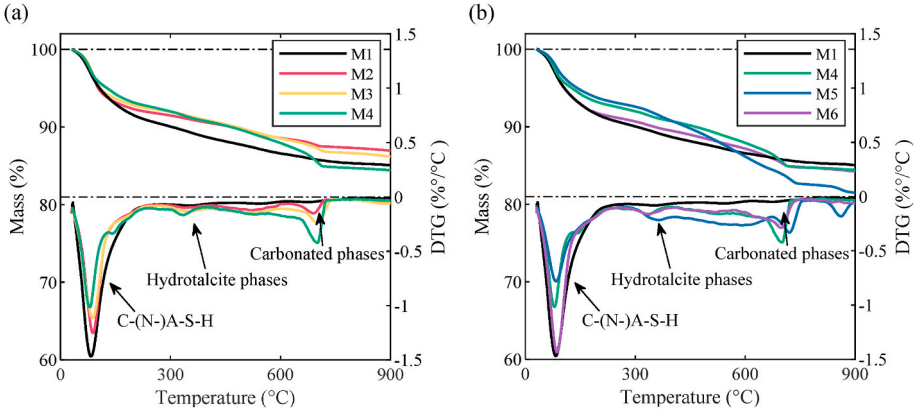

Fig. 11. TG and DTG curves of AA samples (a) AA particles with different MFA content; (b) AA particles with different Ms in activators.

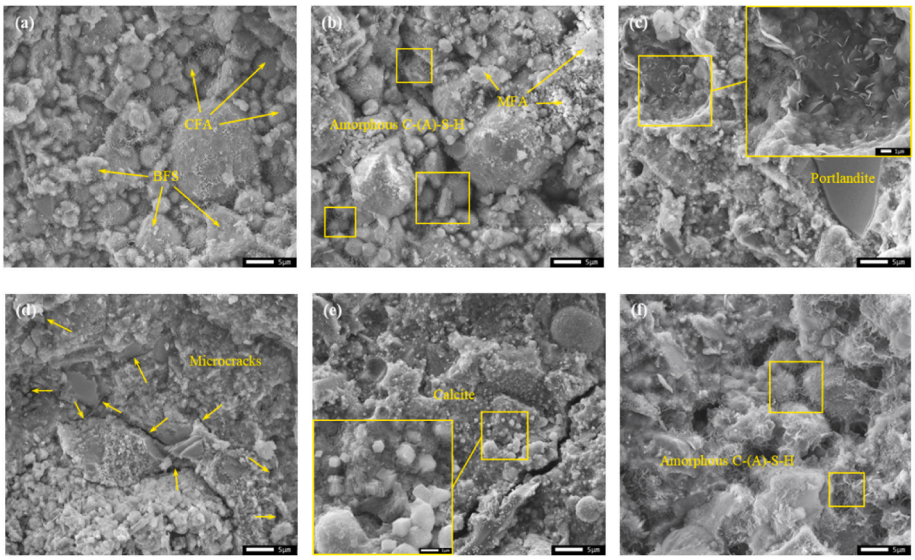

Fig. 12. Representative SEM images (SE mode) on fracture surfaces of hardened AA particles after steam curing (2000 × magnification) (a) M1; (b) M2; (c) M3 (5000 × magnification for the upper corner image); (d) M4; (e) M5; (f) M6.

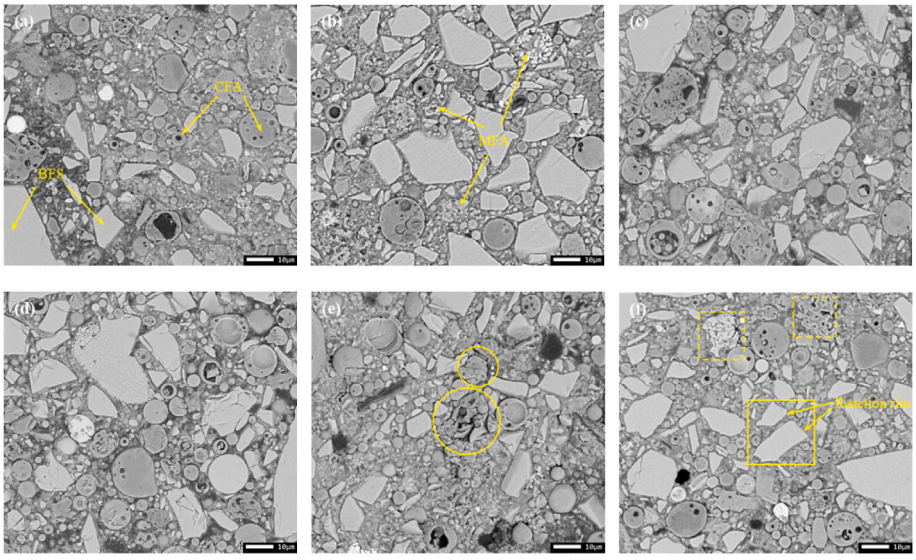

Fig. 13. Representative SEM images (BSE mode) on polished cross sections of hardened AA particles after steam curing (1000 × magnification) (a) M1; (b) M2; (c) M3; (d) M4; (e) M5; (f) M6.

referring to the intensive calcite phases detected in XRD patterns (Fig. 10). Meanwhile, the solid matrix in these mixtures was detected with more microcracks and a higher porosity along with the increase in MFA content, which was confirmed by the reduction in apparent density Table 5. It is noteworthy that portlandite phases featured pseudo-hexagonal morphologies were observed by adopting MFA, which aligned with the corresponding phases detected by XRD analyses (Figs. 6 and 10). Eventually, the amorphous reaction products became predominant again on precursor surfaces in M6 due to the presence of more silicate species in activators, promoting the formation of C-(N)-A-S-H gels (Zhang et al., 2017) (Bernal et al., 2013).

BSE images on polished AA cross sections are presented in Fig. 13. It was found that the precursor grains were tightly packed against each other in the hardened matrix, due to the relatively low w/b applied among all mixtures (Table 2). Solid particles with different morphologies were observed, referring to the undissolved precursor particles. In the meantime, interparticle regions are filled with reaction products with a darker grey color. Apart from that, the black color regions represent voids and microcracks developed in the hardened matrix. Porous cross-sectional features were detected in CFA and MFA particles, which were correlated to the incineration process (Bayuseno and Schmahl, 2010) (Škvára et al., 2009). As indicated by SEM images on precursors (Figs. 3 and 7 (b)), CFA grains exhibit spherical morphology, whereas MFA grains are irregularly shaped. By contrast, BFS grains were observed with a denser matrix, as indicated in Fig. 13(a) and (b). It was observed in all mixtures that BFS grains were tightly embedded in the hardened reaction products, indicating the more reactive nature over CFA and MFA precursors. On the contrary, MFA grains with limited reactivity were observed more detached from the adjacent reaction products, as shown in Fig. 13 (b). It became more pronounced with the increase in MFA content in the mix design, accompanied by a more porous matrix. With the absence of silicate species in activators, clear interfaces between MFA particles and reaction products were observed in Fig. 13 (d), which present as the weak bond to reduce the mechanical

properties of AA particles (Wu et al., 2016) (Gao et al., 2005). M5 in turn exhibited the lowest strength among all mixtures, associated with high water absorption and low specific density characters compared to other AAs (Fig. 8 and Table 5). On the other hand, the matrix of reaction products became apparently denser in M6 by using a higher silicate modulus in the activator, coupled with a less porous and more uniform distribution of reaction products in interparticle regions (Fig. 13 (f)). This is attributed to the presence of more silicate species to promote the dissolution of multiple ions from precursors and thereby facilitate the activation reactions (Puertas et al., 2004a) (Sun et al., 2023). Accordingly, a thick layer of reaction rims was detected in M6 around the reactive BFS grains, as denoted by the solid rectangular in Fig. 13(e) and (f). Instead, MFA grains remained less integrated with the hardened matrix of reaction products (dashed rectangular), due to their less reactive and highly porous natures.

EDX analyses were performed on BSE images shown in Fig. 13 to investigate the chemical composition of interparticle reaction products in hardened AA samples. The average atomic ratios in different AAM mixtures are summarized in Table 7, which were obtained out of at least 15 random spots selected on the BSE image. M1 was detected with the lowest Ca/Si ratio of 0.78 among all mixtures, which gradually increased with a higher MFA content to replace CFA. This is ascribed to the apparently higher calcium content in MFA over CFA as indicated in Table 3. Moreover, the Ca/Si ratio inversely declined in M5 and M6, due to the presence of numerous free silicate species to incorporate calcium cations in the reaction products. Results have further illustrated the negative correlation between the Ca/Si ratio and mechanical strength in AAMs, which is in agreement with earlier studies (Sun et al., 2024a) (Puertas et al., 2004b). As revealed by Kunther et al. (2017), a higher Ca/Si ratio may lead to reductions in surface area and increases in the molar volume of C-S-H phases, declining the mechanical property. Moreover, no apparent variations in the Al/Si ratio were observed by varying the mix design from M1 to M4, since the substitution of CFA with MFA led to significant reductions in both Al_2O_3 and SiO_2 content in the precursor (Table 1). However, the Al/Si ratio gradually declined with more silicate species in the activator, which adversely affected the Al uptake in silicate tetrahedron structures (Myers et al., 2015) (Hôpital et al., 2015). In addition, it was found that the Na/Si ratio slightly improved with a higher Ms in the activator from M4 to M6, which aligns with previous research (Dai et al., 2023). Eventually, the (2Ca+2 Mg + K + Na)/(Si + Al) atomic ratio was calculated to evaluate the cation binding capability of reaction products, as shown in Table 7. As is known that silicate species are interconnected to assemble Si-tetrahedrons, associated with the uptake of Al species to form the aluminosilicate backbone structures in AAMs (Gislason and Oelkers, 2003) (Provis and Van Deventer). On top of that, alkali (Na, K, etc.) and alkali earth (Ca, Mg, etc.) cations are incorporated as modifiers to balance the negative charging sites in reaction products (Duxson and Provis, 2008) (Provis and Van Deventer, 2013). Similarly, previous studies have explored that heavy metals could be incorporated into the AAM structures by substituting the charge-balancing cations in reaction products to achieve chemical s/s. In particular, it has been confirmed that Cd, Cu, Pb, and Zn divalent cations were capable of replacing calcium cations in C-(N-)A-S-H gels due to the similar ionic radius and same valence (Deja, 2002) (Li et al., 2021) (Wang et al., 2025). As illustrated in Table 7, the (2Ca+2 Mg + K + Na)/(Si + Al) ratio progressively increased with an elevated MFA dosage in AAs. It can be inferred that the charge-balancing sites on reaction products became less available due to the more incorporation of alkali and alkali earth cations, which might partially contribute to the increase in heavy metal leaching in M2, M3, and M4. On the contrary, more silicate species originated from the activator were interconnected to the aluminosilicate tetrahedron structures in AAMs to accommodate heavy metal cations (Brough and Atkinson, 2002) (Tian et al., 2020), and thus they were less detected in the leachate of M6 (Table 6).

Table 7
Average atomic ratios in hardened AA samples by EDX analyses.

	Ca/Si	Al/Si	Na/Si	Mg/Al	(2Ca+2 Mg + K + Na)/(Si + Al)
M1	0.78±0.12	0.51±0.06	0.09±0.02	0.33±0.14	1.57±0.17
M2	1.10±0.10	0.53±0.10	0.12±0.03	0.46±0.15	1.89±0.20
M3	1.29±0.19	0.48±0.09	0.13±0.02	0.56±0.12	2.04±0.33
M4	1.31±0.19	0.55±0.04	0.15±0.08	0.57±0.19	2.37±0.29
M5	1.39±0.18	0.62±0.09	0.13±0.02	0.65±0.12	2.49±0.12
M6	1.24±0.09	0.37±0.05	0.27±0.05	0.44±0.15	2.15±0.12

3.6. Discussion and perspectives

The artificial aggregates produced using this pelletization technique demonstrate exceptional potential as a sustainable alternative to natural aggregates for construction applications. Our research reveals that these artificial aggregates not only match but, in certain cases, surpass the mechanical performance of natural aggregates, offering up to 15% greater compressive strength. Meanwhile, the aggregates developed in this study exhibit comparable density and water absorption properties to those reported in previous studies (İpek et al., 2020) (Shang et al., 2022) (Ren et al., 2021), confirming their suitability for a wide range of construction applications. Furthermore, the innovative natural carbonation and alkali activation processes used in their production effectively stabilize and immobilize up to 98% of the heavy metal content found in municipal fly ash (MFA), ensuring adherence to stringent environmental regulations. This dual advantage of environmental remediation and material production positions AAs as a highly promising eco-friendly option.

In addition, the production process supports sustainability goals by transforming industrial waste materials into valuable resources, with studies showing a 30% reduction in landfill reliance and a 25% conservation of natural aggregate resources. This circular economy approach enhances their practicality and attractiveness as a viable replacement for traditional aggregates. However, to fully validate their effectiveness and reliability in real-world scenarios, further research should focus on evaluating their long-term durability under diverse environmental conditions. Large-scale production trials and comparative studies with natural aggregates in various construction contexts are also essential to assess their performance and scalability. These advancements will strengthen their role as a reliable and sustainable solution for modern construction practices.

4. Conclusions

The current study has explored the potential application of municipal solid waste incineration fly ash (MFA) in producing artificial aggregates (AAs) with ternary alkali-activated materials (AAMs). Natural carbonation and alkali activation have been adopted to improve the leaching of heavy metal content embedded in MFA. The effects of MFA content and activator compositions on the properties of AAs were comprehensively investigated. The following conclusions can be drawn according to the results obtained:

- The leaching of Cu, Zn, Cd, Cr, Pb, and Ni heavy metals in MFA was considerably reduced after six-month natural carbonation, accompanied by the formation of numerous calcite phases in carbonated MFA. In addition, the chloride content in KCl, NaCl, and CaClOH forms was effectively removed by washing with water.
- AA generally exhibited higher or comparable strength with respect to natural granite aggregates. It was found that the compressive strength declined by 13.2% with 10 wt% MFA in precursors, and

further reduced with a higher MFA dosage. While the compressive strength of AA gradually improved with a higher silicate modulus in the activator.

- By using alkali activation, the efficiency of Cu, Zn, Cd, and Pb heavy metals solidification/stabilization (s/s) has exceeded 99% in all crushed AA samples. In contrast, alkali activation showed less capability in the s/s of Cr. However, these heavy metals detected in the leachate of AAs were far below the limitation indicated in GB standards.
- MFA inhibited the formation of C-(N)-A-S-H gels as the primary reaction products in AAMs, while the hydrotalcite and carbonated phases were increased with a higher MFA content. This is accompanied by more porous AA particles with microcracks in the matrix, leading to slight increases in heavy metal leaching.

To sum up, the current work has explored a promising approach to utilize MFA, as a hazardous waste material. The AA produced with ternary AAM mixtures not only achieved effective s/s of various heavy metals within the aggregate matrix, but also reached comparable strength as natural aggregates. The method proposed also might assist in mitigating the crisis of natural aggregate resources in the construction sector.

CRediT authorship contribution statement

Jing Gong: Methodology, Investigation. **Mengmeng Wang:** Writing – original draft, Methodology, Investigation. **Guo Yang:** Writing – review & editing, Resources, Investigation. **Han Guo:** Writing – original draft, Methodology, Investigation. **Jie Yao:** Resources, Investigation. **Yaxin Tao:** Writing – review & editing, Methodology, Investigation. **Jing Zhong:** Writing – review & editing, Supervision, Funding acquisition. **Yubo Sun:** Writing – review & editing, Supervision, Methodology, Conceptualization.

Declaration of competing interest

The authors declare that they have no known competing financial interests or personal relationships that could have appeared to influence the work reported in this paper.

Acknowledgments

The present work was funded by the Key Laboratory of Catalysis and Energy Materials Chemistry of Ministry of Education & Hubei Key Laboratory of Catalysis and Materials Science (CHCL19001). In addition, the financial support from the National Natural Science Foundation of China (52408254) is gratefully acknowledged.

Data availability

Data will be made available on request.

References

Ajdukiewicz, A., Kliszczewicz, A., 2002. Influence of recycled aggregates on mechanical properties of HS/HPC. Cem. Concr. Compos. 24 (2), 269–279. https://doi.org/10.1016/S0958-9465(01)00012-9.

Alba, N., Vázquez, E., Gasso, S., Baldasano, J.M., 2001. Stabilization/solidification of MSW incineration residues from facilities with different air pollution control systems. Durability of matrices versus carbonation. Waste Manag. 21 (4), 313–323.

Aslam, M.S., Huang, B., Cui, L., 2020. Review of construction and demolition waste management in China and USA. J. Environ. Manag. 264, 110445. https://doi.org/10.1016/j.jenvman.2020.110445.

Bayuseno, A.P., Schmahl, W.W., 2010. Understanding the chemical and mineralogical properties of the inorganic portion of MSWI bottom ash. Waste Manag. 30 (8–9), 1509–1520. https://doi.org/10.1016/j.wasman.2010.03.010.

Behera, M., Bhattacharyya, S.K., Minocha, A.K., Deoliya, R., Maiti, S., 2014. Recycled aggregate from C&D waste & its use in concrete–A breakthrough towards sustainability in construction sector: a review. Construct. Build. Mater. 68, 501–516.

Ben Haha, M., Lothenbach, B., Le Saout, G., Winnefeld, F., 2011a. Influence of slag chemistry on the hydration of alkali-activated blast-furnace slag - Part I: effect of MgO. Cement Concr. Res. 41 (9), 955–963. https://doi.org/10.1016/j.cemconres.2011.05.002.

Ben Haha, M., Le Saout, G., Winnefeld, F., Lothenbach, B., 2011b. Influence of activator type on hydration kinetics, hydrate assemblage and microstructural development of alkali activated blast-furnace slags. Cement Concr. Res. 41 (3), 301–310. https://doi.org/10.1016/j.cemconres.2010.11.016.

Ben Haha, M., Lothenbach, B., Le Saout, G.L., Winnefeld, F., 2011c. Influence of slag chemistry on the hydration of alkali-activated blast-furnace slag—Part I: effect of MgO. Cement Concr. Res. 41 (9), 955–963.

Bernal, S.A., et al., 2013. Gel nanostructure in alkali-activated binders based on slag and fly ash, and effects of accelerated carbonation. Cement Concr. Res. 53, 127–144. https://doi.org/10.1016/j.cemconres.2013.06.007.

Blengini, G.A., et al., 2012. Life cycle assessment guidelines for the sustainable production and recycling of aggregates: the sustainable aggregates resource management project (SARMa). J. Clean. Prod. 27, 177–181.

Brough, A.R., Atkinson, A., 2002. Sodium silicate-based, alkali-activated slag mortars: Part I. Strength, hydration and microstructure. Cement Concr. Res. 32 (6), 865–879.

Butler, L., West, J.S., Tighe, S.L., 2011. The effect of recycled concrete aggregate properties on the bond strength between RCA concrete and steel reinforcement. Cement Concr. Res. 41 (10), 1037–1049. https://doi.org/10.1016/j.cemconres.2011.06.004.

C. Ag- and B. C. 127-15 Statements, "SAg-, C. and Statements, B. [no date]. Standard Test Method for Relative Density (Specific Gravity) and Absorption of Coarse., pp. 1–5. doi: 10.1520/C0127-15.2.tandard Test Method for Relative Density (Specific Gravity) and Absorption of Coarse," pp. 1–5, doi: 10.1520/C0127-15.2.

Cao, R., Zhang, S., Banthia, N., Zhang, Y., Zhang, Z., 2020. Interpreting the early-age reaction process of alkali-activated slag by using combined embedded ultrasonic measurement, thermal analysis, XRD, FTIR and SEM. Compos. Part B Eng. 186 (January), 107840. https://doi.org/10.1016/j.compositesb.2020.107840.

Chen, J., et al., 2022. Study on the accelerated carbonation of MSWI fly ash under ultrasonic excitation: CO2 capture, heavy metals solidification, mechanism and geochemical modelling. Chem. Eng. J. 450, 138418.

Chen, B., Perumal, P., Illikainen, M., Ye, G., 2023a. A review on the utilization of municipal solid waste incineration (MSWI) bottom ash as a mineral resource for construction materials. J. Build. Eng. 71, 106386. https://doi.org/10.1016/j.jobe.2023.106386.

Chen, J., et al., 2023b. Accelerated carbonation of ball-milling modified MSWI fly ash: migration and stabilization of heavy metals. J. Environ. Chem. Eng. 11 (2), 109396.

Cheng, H., Hu, Y., 2010. Municipal solid waste (MSW) as a renewable source of energy: current and future practices in China. Bioresour. Technol. 101 (11), 3816–3824.

Cheng, J., Chen, M., Tang, S., 2023. Shenzhen–A typical benchmark of Chinese rapid urbanization miracle. Cities 140, 104421.

Dai, X., Tao, Y., Van Tittelboom, K., De Schutter, G., 2023. Rheological and mechanical properties of 3D printable alkali-activated slag mixtures with addition of nano clay. Cem. Concr. Compos. 139, 104995.

Deja, J., 2002. Immobilization of Cr6+, Cd2+, Zn2+ and Pb2+ in alkali-activated slag binders. Cem. Concr. Res., vol. 32 (12), 1971–1979. https://doi.org/10.1016/S0008-8846(02)00904-3.

Duxson, P., Provis, J.L., 2008. Designing precursors for geopolymer cements. J. Am. Ceram. Soc. 91 (12), 3864–3869. https://doi.org/10.1111/j.1551-2916.2008.02787.x.

Duxson, P., Provis, J.L., Lukey, G.C., Mallicoat, S.W., Kriven, W.M., Van Deventer, J.S.J., 2005. Understanding the relationship between geopolymer composition, microstructure and mechanical properties. Colloids Surfaces A Physicochem. Eng. Asp. 269 (1–3), 47–58. https://doi.org/10.1016/j.colsurfa.2005.06.060.

Fan, C., Wang, B., Zhang, T., 2018. Review on cement stabilization/solidification of municipal solid waste incineration fly ash. Adv. Mater. Sci. Eng. 2018 (1), 5120649.

Fan, P., et al., 2020. The spatial restructuring and determinants of industrial landscape in a mega city under rapid urbanization. Habitat Int. 95, 102099.

Fan, C., Wang, B., Ai, H., Qi, Y., Liu, Z., 2021. A comparative study on solidification/stabilization characteristics of coal fly ash-based geopolymer and Portland cement on heavy metals in MSWI fly ash. J. Clean. Prod. 319, 128790.

Fan, C., Ding, W., Wang, B., 2024. Solidification/stabilization and optimization of municipal solid waste incineration fly ash with aluminosilicate solid wastes. J. Environ. Manag. 357, 120825.

Gao, J.M., Qian, C.X., Liu, H.F., Wang, B., Li, L., 2005. ITZ microstructure of concrete containing GGBS. Cement Concr. Res. 35 (7), 1299–1304.

Gao, Y., Jiang, Y., Tao, Y., Shen, P., Poon, C.S., 2024. Accelerated carbonation of recycled concrete aggregate in semi-wet environments: a promising technique for CO2 utilization. Cement Concr. Res. 180, 107486.

Garcia-Lodeiro, I., Palomo, A., Fernández-Jiménez, A., MacPhee, D.E., 2011. Compatibility studies between N-A-S-H and C-A-S-H gels. Study in the ternary diagram Na2O-CaO-Al2O3-SiO 2-H2O. Cement Concr. Res. 41 (9), 923–931. https://doi.org/10.1016/j.cemconres.2011.05.006.

Gebregziabiher, B.S., Thomas, R., Peethamparan, S., 2015. Very early-age reaction kinetics and microstructural development in alkali-activated slag. Cem. Concr. Compos. 55, 91–102. https://doi.org/10.1016/j.cemconcomp.2014.09.001.

Gesoğlu, M., Özturan, T., Güneyisi, E., 2007. Effects of fly ash properties on characteristics of cold-bonded fly ash lightweight aggregates. Construct. Build. Mater. 21 (9), 1869–1878. https://doi.org/10.1016/j.conbuildmat.2006.05.038.

Gesoğlu, M., Güneyisi, E., Öz, H.Ö., 2012. Properties of lightweight aggregates produced with cold-bonding pelletization of fly ash and ground granulated blast furnace slag. Mater. Struct. 45, 1535–1546.

Gislason, S.R., Oelkers, E.H., 2003. Mechanism, rates, and consequences of basaltic glass dissolution: II. An experimental study of the dissolution rates of basaltic glass as a function of pH and temperature. Geochem. Cosmochim. Acta 67 (20), 3817–3832.
Gong, M., Li, M., Wang, W., Tan, Z., Sun, Y., 2024. Investigation of micromechanics and relaxation spectrum evolution in multiple recycled asphalt binders. Mater. Struct. 57 (7), 1–18.
Habert, G., Bouzidi, Y., Chen, C., Jullien, A., 2010. Development of a depletion indicator for natural resources used in concrete. Resour. Conserv. Recycl. 54 (6), 364–376.
Hôpital, E.L., Lothenbach, B., Le Saout, G., Kulik, D., Scrivener, K., 2015. Cement and concrete research incorporation of aluminium in calcium-silicate-hydrates. Cement Concr. Res. 75, 91–103. https://doi.org/10.1016/j.cemconres.2015.04.007.
Horvath, A., 2004. Construction materials and the environment. Annu. Rev. Environ. Resour. 29, 181–204.
Ioannidou, D., Meylan, G., Sonnemann, G., Habert, G., 2017. Is gravel becoming scarce? Evaluating the local criticality of construction aggregates. Resour. Conserv. Recycl. 126, 25–33. https://doi.org/10.1016/j.resconrec.2017.07.016.
İpek, S., Ayodele, O.A., Mermerdaş, K., 2020. Influence of artificial aggregate on mechanical properties, fracture parameters and bond strength of concretes. Construct. Build. Mater. 238, 117756. https://doi.org/10.1016/j.conbuildmat.2019.117756.
Ismail, I., Bernal, S.A., Provis, J.L., San Nicolas, R., Hamdan, S., van Deventer, J.S.J., 2014. Modification of phase evolution in alkali-activated blast furnace slag by the incorporation of fly ash. Cem. Concr. Compos. 45, 125–135.
Iveson, S.M., Litster, J.D., Hapgood, K., Ennis, B.J., 2001. Nucleation, growth and breakage phenomena in agitated wet granulation processes: a review. Powder Technol. 117 (1–2), 3–39.
Jiang, Y., Ling, T.-C., Shi, M., 2020. Strength enhancement of artificial aggregate prepared with waste concrete powder and its impact on concrete properties. J. Clean. Prod. 257, 120515. https://doi.org/10.1016/j.jclepro.2020.120515.
Kapeluszna, E., Kotwica, Ł., Różycka, A., Gołek, Ł., 2017. Incorporation of Al in CASH gels with various Ca/Si and Al/Si ratio: microstructural and structural characteristics with DTA/TG, XRD, FTIR and TEM analysis. Construct. Build. Mater. 155, 643–653.
Kim, T., 2019. The effects of polyaluminum chloride on the mechanical and microstructural properties of alkali-activated slag cement paste. Cem. Concr. Compos. 96, 46–54. https://doi.org/10.1016/j.cemconcomp.2018.11.010.
Kulasuriya, C., Vimonsatit, V., Dias, W.P.S., De Silva, P., 2014. Design and development of alkali pozzolan cement (APC). Construct. Build. Mater. 68, 426–433.
Kumar, A., Samadder, S.R., 2017. A review on technological options of waste to energy for effective management of municipal solid waste. Waste Manag. 69, 407–422.
Kunther, W., Ferreiro, S., Skibsted, J., 2017. Influence of the Ca/Si ratio on the compressive strength of cementitious calcium–silicate–hydrate binders. J. Mater. Chem. A 5 (33), 17401–17412.
Le Saoût, G., Ben Haha, M., Winnefeld, F., Lothenbach, B., 2011. Hydration degree of alkali-activated slags: a 29 Si nmr study. J. Am. Ceram. Soc. 94 (12), 4541–4547.
Li, Y., et al., 2000. Measurement and statistics of single pellet mechanical strength of differently shaped catalysts. Powder Technol. 113 (1–2), 176–184.
Li, X., et al., 2021. An environment-friendly pretreatment process of municipal solid waste incineration fly ash to enhance the immobilization efficiency by alkali-activated slag cement. J. Clean. Prod. 290, 125728. https://doi.org/10.1016/j.jclepro.2020.125728.
Liang, S., Chen, J., Guo, M., Feng, D., Liu, L., Qi, T., 2020. Utilization of pretreated municipal solid waste incineration fly ash for cement-stabilized soil. Waste Manag. 105, 425–432.
Liu, J., Hu, L., Tang, L., Ren, J., 2021. Utilisation of municipal solid waste incinerator (MSWI) fly ash with metakaolin for preparation of alkali-activated cementitious material. J. Hazard Mater. 402, 123451.
Liu, Y., Wan, W., Lu, J.-X., Poon, C.S., Hu, S., Wang, F., 2023. Preparation of glass-ceramic-based artificial aggregates using multiple solid wastes: crystallization mechanism. J. Clean. Prod. 421, 138298.
Mian, M.M., Zeng, X., Bin Nasry, A. al N., Al-Hamadani, S.M.Z.F., 2017. Municipal solid waste management in China: a comparative analysis. J. Mater. Cycles Waste Manag. 19 (3), 1127–1135.
Myers, R.J., Bernal, S.A., Gehman, J.D., van Deventer, J.S.J., Provis, J.L., 2015. The Role of Al in cross-linking of alkali-activated slag cements. J. Am. Ceram. Soc. 98 (3), 996–1004.
Narattha, C., Chaipanich, A., 2018. Phase characterizations, physical properties and strength of environment-friendly cold-bonded fly ash lightweight aggregates. J. Clean. Prod. 171, 1094–1100. https://doi.org/10.1016/j.jclepro.2017.09.259.
Niu, Y., Wen, L., Guo, X., 2022. Co-disposal and reutilization of municipal solid waste and its hazardous incineration fly ash. Environ. Int. 166, 107346.
Palacios, M., et al., 2021. Cement and Concrete Research Early reactivity of sodium silicate-activated slag pastes and its impact on rheological properties. Cement Concr. Res. 140 (October 2020), 106302. https://doi.org/10.1016/j.cemconres.2020.106302.
Pan, Z., Cheng, L., Lu, Y., Yang, N., 2002. Hydration products of alkali-activated slag–red mud cementitious material. Cement Concr. Res. 32 (3), 357–362. https://doi.org/10.1016/S0008-8846(01)00683-4.
Pan, S.-Y., Du, M.A., Huang, I.-T., Liu, I.-H., Chang, E.E., Chiang, P.-C., 2015. Strategies on implementation of waste-to-energy (WTE) supply chain for circular economy system: a review. J. Clean. Prod. 108, 409–421.
Park, S.-S., Kim, S.-J., Chen, K., Lee, Y.-J., Lee, S.-B., 2018. Crushing characteristics of a recycled aggregate from waste concrete. Construct. Build. Mater. 160, 100–105. https://doi.org/10.1016/j.conbuildmat.2017.11.036.
Peduzzi, P., 2014. Sand, rarer than one thinks. Environ. Dev. 11 (208–218), 682.
Petrillo, A., Colangelo, F., Farina, I., Travaglioni, M., Salzano, C., Cioffi, R., 2022. Multi-criteria analysis for Life Cycle Assessment and Life Cycle Costing of lightweight artificial aggregates from industrial waste by double-step cold bonding palletization. J. Clean. Prod. 351, 131395.
Provis, J.L., Bernal, S.A., 2014. Geopolymers and related alkali-activated materials. Annu. Rev. Mater. Res. 44, 299–327. https://doi.org/10.1146/annurev-matsci-070813-113515.
J. L. Provis and J. S. J. Van Deventer, "RILEM State-Of-The-Art Reports State-Of-The-Art Report, RILEM TC 224-AAM.".
Provis, J.L., Van Deventer, J.S.J., 2013. Alkali Activated Materials: State-Of-The-Art Report, RILEM TC 224-AAM, vol. 13. Springer Science & Business Media.
Puertas, F., Fernández-Jiménez, A., Blanco-Varela, M.T., 2004a. Pore solution in alkali-activated slag cement pastes. Relation to the composition and structure of calcium silicate hydrate. Cement Concr. Res. 34 (1), 139–148.
Puertas, F., Fernández-Jiménez, A., Blanco-Varela, M.T., 2004b. Pore solution in alkali-activated slag cement pastes. Relation to the composition and structure of calcium silicate hydrate. Cement Concr. Res. 34 (1), 139–148. https://doi.org/10.1016/S0008-8846(03)00254-0.
Ramamurthy, K., Harikrishnan, K.I., 2006. Influence of binders on properties of sintered fly ash aggregate. Cem. Concr. Compos. 28 (1), 33–38.
Ren, P., Ling, T.-C., Mo, K.H., 2021. Recent advances in artificial aggregate production. J. Clean. Prod. 291, 125215.
Ren, M., Shen, P., Tao, Y., Poon, C., 2024. Development of highly carbonation-effective calcium silicates (β-C2S): phase evolution, microstructure, and carbonation mechanisms. Cement Concr. Res. 181, 107542.
Rovnaník, P., Bayer, P., Rovnaníková, P., 2013. Characterization of alkali activated slag paste after exposure to high temperatures. Construct. Build. Mater. 47, 1479–1487.
Shang, X., Chang, J., Yang, J., Ke, X., Duan, Z., 2022. Life cycle sustainable assessment of natural vs artificial lightweight aggregates. J. Clean. Prod. 367, 133064. https://doi.org/10.1016/j.jclepro.2022.133064.
Shao, N., Wei, X., Monasterio, M., Dong, Z., Zhang, Z., 2021. Performance and mechanism of mold-pressing alkali-activated material from MSWI fly ash for its heavy metals solidification. Waste Manag. 126, 747–753. https://doi.org/10.1016/j.wasman.2021.04.003.
Shi, M., Ling, T.-C., Gan, B., Guo, M.-Z., 2019. Turning concrete waste powder into carbonated artificial aggregates. Construct. Build. Mater. 199, 178–184. https://doi.org/10.1016/j.conbuildmat.2018.12.021.
Singh, R., Budarayavalasa, S., 2021. Solidification and stabilization of hazardous wastes using geopolymers as sustainable binders. J. Mater. Cycles Waste Manag. 23 (5), 1699–1725.
Škvára, F., Kopecký, L., Šmilauer, V., Bittnar, Z., 2009. Material and structural characterization of alkali activated low-calcium brown coal fly ash. J. Hazard Mater. 168 (2), 711–720. https://doi.org/10.1016/j.jhazmat.2009.02.089.
Song, Q., Deng, S., Ling, T.-C., 2023. Study on the crushing strength improvement of artificial aggregates made with 100% solid wastes using polyvinyl alcohol solution. Construct. Build. Mater. 400, 132576. https://doi.org/10.1016/j.conbuildmat.2023.132576.
Stegemann, J.A., Schneider, J., Baetz, B.W., Murphy, K.L., 1995. Lysimeter washing of MSW incinerator bottom ash. Waste Manag. Res. 13 (2), 149–165.
Sun, Y., et al., 2022. Rheology of alkali-activated slag pastes: new insight from microstructural investigations by cryo-SEM. Cement Concr. Res. 157 (April), 106806. https://doi.org/10.1016/j.cemconres.2022.106806.
Sun, Y., et al., 2023. Cement and Concrete Research Interpretation of the early stiffening process in alkali-activated slag pastes. Cement Concr. Res. 167 (November 2022), 107118. https://doi.org/10.1016/j.cemconres.2023.107118.
Sun, Y., et al., 2024a. A conceptual design of two-stream alkali-activated materials. Cem. Concr. Compos. 148, 105485. https://doi.org/10.1016/j.cemconcomp.2024.105485.
Sun, Y., Mohan, M.K., Dai, X., Zhang, Y., Ye, G., De Schutter, G., 2024b. Effects of mixing conditions and activator anionic species on the rheology of silicate-activated slag concrete. Cem. Concr. Compos. 150, 105556.
Tang, P., Xuan, D., Poon, C.S., Tsang, D.C.W., 2019. Valorization of concrete slurry waste (CSW) and fine incineration bottom ash (IBA) into cold bonded lightweight aggregates (CBLAs): feasibility and influence of binder types. J. Hazard Mater. 368, 689–697. https://doi.org/10.1016/j.jhazmat.2019.01.112.
Tian, X., Rao, F., Leon-Patino, C.A., Song, S., 2020. Co-disposal of MSWI fly ash and spent caustic through alkaline-activation: immobilization of heavy metals and organics. Cem. Concr. Compos. 114, 103824.
Wang, L., Jin, Y., Nie, Y., 2010a. Investigation of accelerated and natural carbonation of MSWI fly ash with a high content of Ca. J. Hazard Mater. 174 (1), 334–343. https://doi.org/10.1016/j.jhazmat.2009.09.055.
Wang, L., Jin, Y., Nie, Y., 2010b. Investigation of accelerated and natural carbonation of MSWI fly ash with a high content of Ca. J. Hazard Mater. 174 (1), 334–343. https://doi.org/10.1016/j.jhazmat.2009.09.055.
Wang, H., et al., 2023. Effect of raw material ratio and sintering temperature on properties of coal gangue-feldspar powder artificial aggregate. Construct. Build. Mater. 384, 131400.
Wang, X., Yin, Z.-Y., Wu, W., Zhu, H.-H., 2025. Neural network-augmented differentiable finite element method for boundary value problems. Int. J. Mech. Sci. 285, 109783.
Wei, Y., Liu, S., Yao, R., Chen, S., Gao, J., Shimaoka, T., 2022. Removal of harmful components from MSWI fly ash as a pretreatment approach to enhance waste recycling. Waste Manag. 150, 110–121. https://doi.org/10.1016/j.wasman.2022.06.041.
Wong, H.S., Buenfeld, N.R., 2006. Patch microstructure in cement-based materials: fact or artefact? Cement Concr. Res. 36 (5), 990–997. https://doi.org/10.1016/j.cemconres.2006.02.008.

Wu, K., Shi, H., Xu, L., Ye, G., De Schutter, G., 2016. Microstructural characterization of ITZ in blended cement concretes and its relation to transport properties. Cement Concr. Res. 79, 243–256. https://doi.org/10.1016/j.cemconres.2015.09.018.
Xiao, J., Xiao, J., 2018. Recycled Aggregate Concrete. Springer.
Xin, M., et al., 2022. Stabilized MSW incineration fly ash co-landfilled with organic waste: leaching pattern of heavy metals and related influencing factors. Process Saf. Environ. Protect. 165, 445–452.
Yan, K., Gao, F., Sun, H., Ge, D., Yang, S., 2019. Effects of municipal solid waste incineration fly ash on the characterization of cement-stabilized macadam. Construct. Build. Mater. 207, 181–189.
Zhang, S., Keulen, A., Arbi, K., Ye, G., 2017. Waste glass as partial mineral precursor in alkali-activated slag/fly ash system. Cement Concr. Res. 102, 29–40. https://doi.org/10.1016/j.cemconres.2017.08.012. November 2016.
Zhang, P., et al., 2020. Self-cementation solidification of heavy metals in lead-zinc smelting slag through alkali-activated materials. Construct. Build. Mater. 249, 118756.
Zhang, X., et al., 2021a. UV/peroxymonosulfate process for degradation of chloral hydrate: pathway and the role of radicals. J. Hazard Mater. 401, 123837.
Zhang, S., Li, Z., Ghiassi, B., Yin, S., Ye, G., 2021b. Fracture properties and microstructure formation of hardened alkali-activated slag/fly ash pastes. Cement Concr. Res. 144, 106447.
Zhang, X., Sun, Y., Zhang, Q., Tian, W., Khan, E., Tsang, D.C.W., 2024. Leaching characteristics of nutrients in food waste digestate-derived biochar. Bioresour. Technol. 399, 130634.
Zheng, L., Wang, C., Wang, W., Shi, Y., Gao, X., 2011. Immobilization of MSWI fly ash through geopolymerization: effects of water-wash. Waste Manag. 31 (2), 311–317. https://doi.org/10.1016/j.wasman.2010.05.015.